Publication III

A. Lankinen, T. Tuomi, M. Karilahti, Z.R. Zytkiewicz, J.Z. Domagala, P.J. McNally, Y-T. Sun, F. Olsson and S. Lourdudoss, *Crystal Defects and Strain of Epitaxial InP Layers Laterally Overgrown on Si*, Crystal Growth & Design **6** (2006) 1096–1100.

© 2006 American Chemical Society

CRYSTAL GROWTH & DESIGN
2006
VOL. 6, NO. 5
1096−1100

Crystal Defects and Strain of Epitaxial InP Layers Laterally Overgrown on Si

A. Lankinen,* T. Tuomi, and M. Karilahti†

Optoelectronics Laboratory, Helsinki University of Technology, P.O. Box 3500, FIN-02015 TKK, Finland

Z. R. Zytkiewicz and J. Z. Domagala

Institute of Physics, Polish Academy of Sciences, Al. Lotnikow 32/46, 02-668 Warsaw, Poland

P. J. McNally

Research Institute for Networks and Communications Engineering, Dublin City University, Dublin 9, Ireland

Y-T. Sun, F. Olsson, and S. Lourdudoss

School of Information and Communication Technology, KTH, Electrum 229, S-164 40 Kista, Sweden

Received July 13, 2005; Revised Manuscript Received February 22, 2006

ABSTRACT: Defects in epitaxial laterally overgrown (ELO) InP layers are examined by high-resolution X-ray diffraction and synchrotron X-ray back-reflection and transmission topography. X-ray diffraction maps produce information about the overall crystal quality of the epitaxial layers in the InP ELO sample. The topographs show small angle boundaries, and the associated dislocations are located at the boundaries between the crystallites; allowing for their relative tilt, the maximum value for this is 0.06°. No defects inside the crystallites can be seen in the topographs, except for a small bending of 0.04° at most, of the ELO lattice planes. The section topographs show deformed X-ray interference fringes resulting from the large strain of the silicon lattice below the seeding areas.

Introduction

The integration of photonic components on silicon-based devices requires good quality epitaxial layers of a direct band gap semiconductor on Si. The lattice mismatch between the readily available direct band gap semiconductors and Si makes it difficult to achieve monocrystalline layers of the epitaxial direct band gap material perfect enough to be used for electronic devices. Epitaxial lateral overgrowth (ELO) is one of the methods commonly used to overcome this problem. For a review of ELO technology, see ref 1.

In this work, the crystal quality and strain structure of an InP ELO layer grown by low-pressure hydride vapor phase epitaxy on silicon is studied with synchrotron radiation X-ray topography and high resolution X-ray diffraction (HRXRD). The growth process and crystal structure of a similar InP ELO layer structure have been previously studied in ref 2, and this study advances further the characterization of crystal properties of the InP ELO layer.

HRXRD measurements and synchrotron X-ray topography[3] are nondestructive methods for studying high-quality crystalline materials. HRXRD is best suited for acquiring accurate average lattice constants and lattice orientations of macroscopic volumes of the sample, whereas topography is used to obtain data on the spatial structure of the crystal defects and the strain fields in the sample. The InP ELO layers were studied with both of these methods to reveal the crystal defects and strain fields of the epitaxial layer and the Si substrate.

* To whom correspondence should be addressed. E-mail: aapo.lankinen@hut.fi.
† Present address: Nokia Oyj, P.O. Box 100, FI-00045 Nokia Group.

Experimental Section

The ELO samples consisted of a (001) Si substrate 4° off-oriented toward ⟨110⟩, a GaAs buffer having a thickness of 0.5 μm, and a 1.5-μm-thick InP seed layer coated by a 70-nm-thick Si_3N_4 mask. The effect of a GaAs buffer between the Si substrate and an epitaxial InP layer has been studied in ref 4. A grid of parallel, 5-μm-wide seeding lines was opened parallel to a direction 60° off the [110] direction in the mask. Subsequently, the InP ELO layer grew from the vapor phase at 620 °C from these openings in the form of 55-μm-wide and 21-μm-thick stripes on the silicon substrate covered by the thin GaAs buffer, the thin InP buffer, and the very thin nitride mask. Figure 1 shows a cross-sectional schematic drawing of one of the ELO stripes. The spacing of the seeding lines was 400 μm; hence, the ELO stripes were too narrow to be in a direct contact with each other.

X-ray diffraction (XRD) curves of the ELO sample were measured in either double or triple axis diffractometer modes. In the double axis mode, the diffracted beam intensity was measured with an open detector as a function of the incoming X-ray beam angle ω, measured from the sample surface. Even though the ω angle is accurate due to the Ge-220 four-crystal monochromator after the X-ray tube ($\Delta\omega \approx 12$ arcsec), the accuracy of the open detector method is quite poor because the 2θ angle between the incoming X-ray beam and the diffracted beam has a fairly large angle of acceptance for the detected X-rays (about 1°). However, the configuration allows a simultaenous measurement of less perfect layers, such as buffer layers, and high-quality layers.

HRXRD maps were measured in the triple axis diffractometer mode. In the triple axis mode, there is an additional analyzer crystal in front of the detector, which allows accurate results for both the ω and 2θ angles. The HRXRD angular space maps display the lattice plane displacement limited $2\theta - \omega$ diffraction curves on one axis and the ω diffraction curves revealing lattice plane orientations on the other.

In addition to the XRD measurements, synchrotron X-ray back-reflection and transmission topography techniques, both in large area and section geometries, were used to study crystalline perfection of the ELO InP layers and the Si substrate. For a review of synchrotron X-ray topography of electronic materials, see for example, ref 5.

10.1021/cg0503301 CCC: $33.50 © 2006 American Chemical Society
Published on Web 04/08/2006

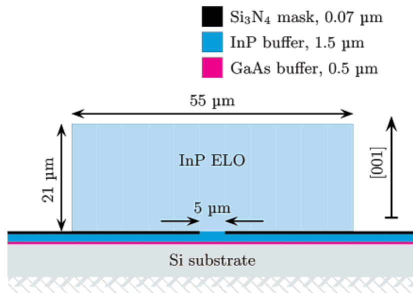

Figure 1. Schematic drawing of the cross-section of one of the InP ELO stripes on the substrate. The drawing is to exact scale, except that the Si_3N_4 mask is drawn 7 times thicker for visibility reasons.

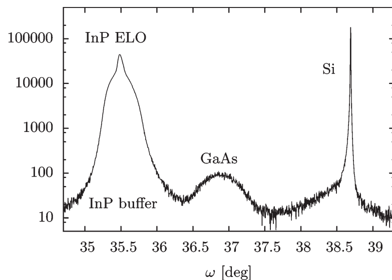

Figure 2. 004 XRD curve of InP ELO sample. Si substrate peak, GaAs buffer peak, InP buffer peak, and InP ELO peak are labeled. The narrow high-intensity part and wide low-intensity part of the InP peak originate from the InP ELO layer and InP buffer, respectively. The offset between ω and θ angles is 3.87°.

Topographs were made at the topography station F1 of the Hamburger Synchrotronstrahlungslabor (HASYLAB) at the Deutsches Elektronen-Synchrotron (DESY) in Hamburg using the continuous spectrum of radiation emitted by a bending magnet source on the DORIS storage ring. The positron momentum was 4.436 GeV/c, and the current ranged from 94 to 143 mA. The sample was set perpendicularly to the incident beam. Diffraction patterns of several high-resolution topographs were recorded on high-resolution GEOLA VRP-M films set 50 mm in front of or behind the sample in the back-reflection and the transmission geometry, respectively. The ELO stripes were vertical in both geometries, and they were on the film side. For the section topography, the beam was narrowed by a horizontal slit having a width of 15 μm. A typical exposure was 400 mA min in the large-area mode and 4000 mA min in the section mode.

Results and Discussion

HRXRD Lattice Maps. Figure 2 shows a typical XRD curve for the InP-Si ELO sample. The Si substrate peak, GaAs buffer peak, InP buffer peak, and InP ELO peaks are all visible and can all be distinguished from each other. The 3.87° offset between ω and θ is caused mainly by the 4° miscut in the Si substrate. Because the GaAs buffer peak has quite a small intensity and is very wide (fwhm is about 0.46°), it is believed that the GaAs buffer layer is strongly textured polycrystalline media. Therefore, it appears that any strain caused by lattice mismatches in the GaAs buffer layer has been relaxed, but some thermal-induced strain probably occurs. Thermally induced strain in GaAs and InP layers on Si after growth has been reported in refs 6 and 7.

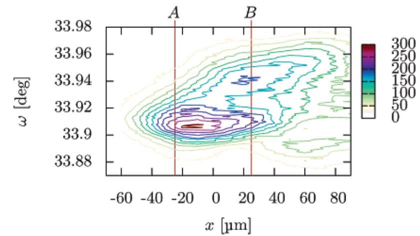

Figure 3. 004 XRD map of InP ELO sample. The map shows how the ω diffraction curves change as a function of displacement x perpendicular to the ELO stripes. The origin of the displacement x is approximately in the middle of the ELO stripe. The ELO stripes have two different regions: the region around omega scan at $x = A \approx -25$ μm with only one crystal orientation and the region around omega scan at $x = B \approx 25$ μm with two possible crystal orientations.

Figure 3 displays a series of triple axis HRXRD ω diffraction curves as a two-dimensional map, in which the diffraction curves are plotted against displacement x of the beam, which is measured along the sample surface and perpendicular to the ELO stripes. The 2θ angle is fixed to the actual value of the InP ELO layer of the sample, which makes the measurement setup very sensitive to the orientational changes of the InP ELO (004) crystal planes. When the X-ray beam first hits the left edge of an ELO stripe, where $x < 0$ μm, the (004) lattice planes of the InP ELO layer have only one orientation. However, on the right side of the ELO stripe, where $x > 0$ μm, there appears to be two different (004) lattice plane orientations in the InP ELO layer. This indicates that the ELO stripes are divided into two regions; the crystallites on one side of the ELO ridge have only one orientation, whereas on the other side they have two possible orientations.

Figure 4 displays a HRXRD angular space map of the InP buffer and InP ELO layers of the sample. The angular space map shows that there is a difference between the InP lattice constants of these two layers in the [001] direction. The measured lattice constants $a_\perp$ of InP ELO, bulk InP from the literature and the InP buffer layer are 5.86713, 5.8687, and 5.87261 Å, respectively. From these values, it can be concluded that the InP ELO layer is under tensile strain in the direction parallel to the sample surface, whereas the InP buffer layer is under compressive strain in the direction parallel to the sample surface.

Table 1 collects some of the measured XRD data and also shows bulk material data for Si, GaAs, and InP for comparison. The InP values are from the angular space map of Figure 4, and the GaAs and Si fwhm values are extracted from the XRD curve of Figure 2.

Synchrotron X-ray Topographs: Crystal Defects within ELO Layers. Figure 5 shows a 004 large-area back-reflection topograph of the InP-Si ELO sample. The topograph displays both the images of the InP ELO layers, marked with E, and their shadows at the seeding lines on the Si substrate image, marked with S. The image of the strain field produced by an empty growth window, where no InP growth occurred, is marked with W. The image of the empty growth window consists of two narrow vertical lines, corresponding to the two strain fields produced by the two edges of the growth window. The tilt between the InP ELO layer lattice and the Si substrate lattice causes a shift, which is marked with vector $\vec{M}$, between the image of the ELO layer and its shadow on the substrate background. Using the sample-to-film distance 50 mm, vector

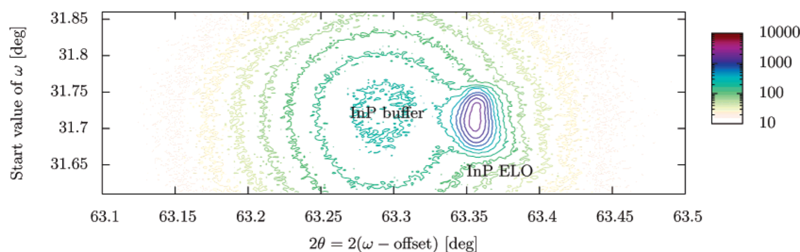

Figure 4. HRXRD angular space map of 004 crystal planes in InP ELO sample. The InP buffer peak and InP ELO peak are identified on the map. The InP ELO peak is centered at $2\theta = 63.3566°$, $\omega = 31.7177°$, and it has fwhm values of $W_{2\theta} = 0.014°$ and $W_\omega = 0.057°$. The InP buffer peak is centered at $2\theta = 63.2906°$, $\omega = 31.6847°$, and it has fwhm values of $W_{2\theta} = 0.136°$ and $W_\omega = 0.197°$.

Table 1. XRD Data Measured from the InP ELO Sample and Related Bulk Material Values from Literature

	2θ	ω fwhm	2θ fwhm	$a_\perp$ [Å]
InP ELO	63.35660°	0.057°	0.01441°	5.86713
InP buffer	63.29060°	0.197°	0.13617°	5.87261
GaAs buffer		1.14556°		
Si substrate		0.01733°		
InP	63.33769°			5.8687
GaAs	66.04842°			5.65325
Si	69.12723 °			5.431

$\vec{M}$ length measured from the topograph, the diffraction vector $\vec{g}$ and the diffraction Miller indices 004 a straightforward calculation gives the value 0.26° of the tilt between the InP ELO layer lattice and Si substrate lattice (001) planes.

Other interesting features visible in the back-reflection topographs of Figure 5 include the InP ELO layer defect images, which are clearly visible in the enlargement in Figure 5. Even though the ELO layer stripes are not perfect single crystals, they consist of crystallites of almost exactly the same orientation. The crystallites are distinguished from each other only by small rotations of the lattices and corresponding small angle boundaries, some of which are marked with B in the enlargement of Figure 5. There are no visible defects inside the fairly large crystallites of the ELO layers.

The crystallite lattices of the InP ELO layer are slightly misoriented from each others. Δx is the width of the zigzag path of the left edge of the ELO crystallite images in the enlargement of Figure 5. A straightforward calculation connects Δx to the angular rotation α of the ELO layer crystallite lattices around the growth window stripe axis, giving a value of 0.06° for the maximum tilt angle α_{MAX}. In addition to the zigzag width Δx between the crystals, there is also some broadening of the image width w of the individual crystallites compared to the width of the layer shadows (see enlargement in Figure 5). This indicates some bending of lattice planes inside the ELO crystallites. The maximum value of the crystallite bending β was calculated from the maximum value of w measured from the topograph, resulting in $\beta_{MAX} = 0.04°$. The total maximum angular broadening of the images resulting from these two partially overlapping effects was also calculated from the topograph to be 0.08° = 288 arcsec, which is slightly more than one would expect from an angular broadening in the HRXRD curves. The angular broadening measured with HRXRD is smaller because the fwhm value obtained by HRXRD averages out the extremities of the lattice defects over the macroscopic volume of the crystal. The averaged fwhm value W_ω produced by the HRXRD measurements was 0.057° = 205 arcsec. Thus, there is a good agreement between the synchrotron X-ray topography and the HRXRD results.

Synchrotron X-ray Topographs: Strain Fields. Figure 6 shows a back-reflection section topograph of the ELO layers and the substrate. The strain fields in the substrate wafers are clearly visible in the topographs; their images reside under the white shadows of the ELO layers marked by S in the topograph. Near the center of the ELO openings, there are hardly visible dark small dots. These dots are images of the strain enhancement caused by the 5-μm-wide growth windows. The stronger strain field images around the white ELO layer shadows originate from the 22-μm-thick and 55-μm-wide ELO layer edges. This shows that the InP ELO layer strains the Si substrate through the 70-nm-thick silicon nitride mask, 1.5-μm-thick InP buffer layer, and 0.5-μm-thick GaAs buffer layer. So, the strain caused by the ELO structure consists of three components: the strain caused by the left side wing of the ELO layer, the strain caused by the right side wing of the ELO layer, and the strain caused by the 5-μm-wide growth window itself. However, when the ELO layer is present (marked by the S-arrows), the strain produced by the growth window appears to be considerably smaller than the strain of a growth window without the ELO layer (marked by the W arrow).

Figure 7 shows a 713 transmission section topograph of the sample, in which the strain fields inside the substrate are very clear. The topograph further demonstrates that the strain fields caused by the ELO layers and the growth windows penetrate very deep into the substrate. The strain field images in the 713 transmission section topograph are composed of three easily distinguishable sections, similar to the 015 back-reflection section topograph of Figure 6. However, the image (marked with W) of the strain originating from the growth window itself is far more clear in the transmission topograph of Figure 7.

Figure 8a−c concentrates on a particular InP ELO stripe on the sample. Figure 8 c shows an enlargement of the leftmost ELO stripe S and its strain field in the 713 transmission section topograph of Figure 7. A schematic drawing of the ELO layer and its growth window are overlayed into the topograph of Figure 8c to make the connection between the ELO stripe and three distinguishable main components of the strain field (marked with arrows) easier to visualize. In addition to the three black contrast areas, there is a clearly visible ring in the outer limit of the strain field. Inside this ring, some X-ray interference maxima and minima are visible, indicating at least partially dynamical imaging in the topograph.

Figure 8a,b shows optical micrographs of the same ELO stripe as the topograph in Figure 8c. From the cross-section micrograph b, it is seen that the bottom of the ELO stripe is attached to the Si substrate through the Si_3N_4 mask and the buffer layers, which the topographs in Figures 6 and 8c also showed. Thus, it is believed that the difference between the thermal expansion

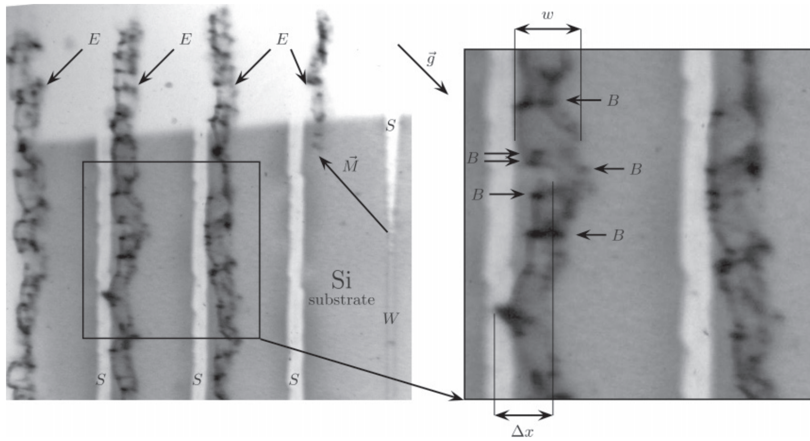

Figure 5. 004 large-area back-reflection topograph of InP ELO sample. Images of the InP ELO layers and their shadows are marked by *E* and *S*, respectively. The shadows appear white, because the topograph is printed as a negative, as they are traditionally displayed. An image of an empty growth window is marked with *W*. Vector $\vec{M}$ represents the image shift due to tilt between the InP ELO layer lattice and the Si substrate lattice, on which the ELO layer shadow resides. Δx is the width of the zigzag path of the left edge of the ELO crystallite images. Small angle boundaries of crystallites are marked with *B*, and $\vec{g}$ is the diffraction vector.

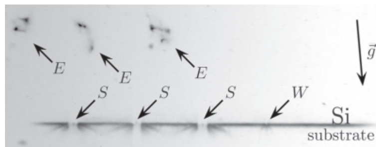

Figure 6. 015 back-reflection section topograph of the InP ELO sample and the related diffraction vector $\vec{g}$. Images of ELO layers and their shadows are marked by *E* and *S*, respectively. An empty growth window without an ELO layer is marked with *W*.

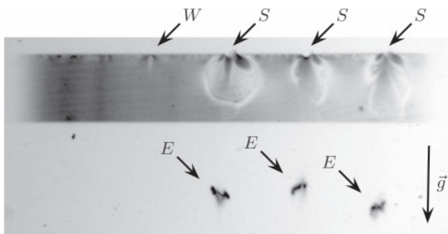

Figure 7. 713 transmission section topograph of InP ELO sample and the related diffraction vector $\vec{g}$. Images of ELO layers and their strain fields in the Si substrate are marked by *E* and *S*, respectively. An empty growth window without an ELO layer is marked with *W*.

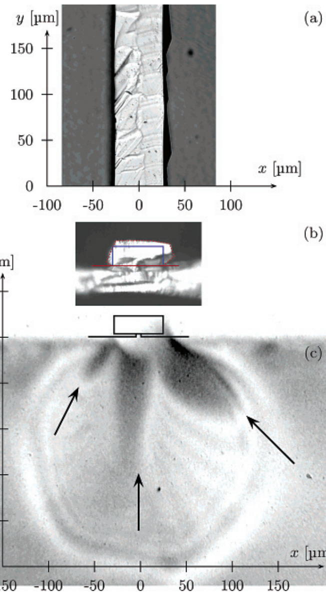

Figure 8. (a) An optical micrograph of an ELO stripe photographed above the sample, (b) an optical section micrograph of the stripe in the same scale, and (c) an enlargement of a 713 transmission section topograph of the ELO stripe showing strain fields in the Si substrate in the same scale as the micrographs above. Three main components of the strain field images are marked with arrows. ELO layer and window opening in the mask are also drawn exactly in the same scale on top of the topographic image. Image size of the topograph is 417 × 305 μm.

coefficients of InP and Si creates the strain in the structure when the sample is cooled after growth. The top view micrograph in Figure 8a shows how the left side of the stripe is rougher than the relatively smooth right side. The roughness is related to the partly strain-relaxed left side of the ELO stripe in Figure 8c, where the strain relaxation is seen as a smaller X-ray intensity on the left side of the stripe image. The strain relaxation is also believed to be related to the secondary crystal orientation observed in the right side of the XRD map of Figure 3, where the orientation of the sample is mirrored with respect to that of Figure 8.

The 311 transmission topograph of Figure 9 shows Pendellösung fringes in the substrate image. The Pendellösung fringes

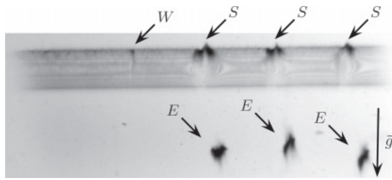

Figure 9. 311 transmission section topograph of InP ELO sample and related diffraction vector $\vec{g}$. Images of ELO layers and their strain fields in the Si substrate are marked by *E* and *S*, respectively. An empty growth window without an ELO layer is marked with *W*.

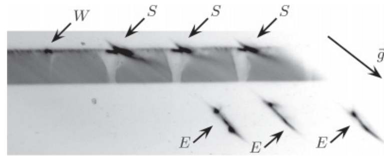

Figure 10. 242 transmission section topograph of InP ELO sample and the related diffraction vector $\vec{g}$. Images of ELO layers and their strain fields in the Si substrate are marked by *E* and *S*, respectively. An empty growth window without an ELO layer is marked with *W*.

are distorted in the strained regions of the sample, especially due to the strain induced by the InP ELO layers. Also, in this topograph the growth window strain field image *W* is the clearest.

The ELO layer images in the 242 transmission section topograph of Figure 10 are heavily stretched along the $\vec{g}$ vector direction. This implies that the (242) lattice planes of the ELO crystals are distorted more than the (311) lattice planes imaged in topograph 311 of Figure 9. A comparison between the diffraction vectors $\vec{g}$ of different diffractions and the ELO stripe directions shows that lattice planes having a diffraction vector $\vec{g}$ parallel to the ELO stripes have very little distortion, whereas topographs imaging lattice planes having their normal nonparallel to the ELO stripes, such as topograph 242 in Figure 10, are heavily distorted.

The anisotropy of the distortion in the ELO layer topographs with respect to the direction of the ELO stripes implies that the ELO layer crystals are strained in the direction perpendicular to the stripes, but not so in the direction parallel to the stripes. The strain occurring in the direction parallel to the stripes is believed to have been relieved by the small angle boundaries observed in the large-area back-reflection topograph of Figure 5. As the ELO layer does not have small angle boundaries in the direction perpendicular to the stripes, the strain in that direction cannot be relieved, which results in bending of the lattices.

The strain fields in the Si substrate are caused by the interface strain perpendicular to the ELO stripes. This can be further confirmed by the 242 transmission section topograph of Figure 10, where the substrate image is heavily distorted below the ELO layer windows (places marked with *S*). Topographs of Figures 7 and 9 having a diffraction vector $\vec{g}$ parallel to the ELO stripes do not show such distortion for the substrate.

Conclusion

We confirm that InP ELO layers on Si have a good overall quality, notwithstanding certain lattice defects. The small angle boundaries and the related maximum tilt of 0.06° together with the maximum bending of 0.04° of the crystallites are quite minor defects, but they still may have a significant impact on the performance and yield of devices produced on the ELO material. Despite the defects revealed by synchrotron X-ray topography, the ELO material has good HRXRD characteristics, because the total maximum angular misorientation of the ELO lattice planes (only 0.08° = 288 arcsec) broadens the HRXRD fwhm values only very slightly.

It appears that X-ray diffraction topography using synchrotron radiation is a method ideally suited for characterizing high-quality heteroepitaxial ELO layers because other methods cannot give accurate information of the spatial strain structure of the crystal layers. HRXRD can be used to characterize the overall quality of the ELO layer, but due to the importance of local strain in the heteroepitaxial ELO structures, X-ray topography can give significantly more elaborate results. However, with HRXRD it is possible to observe the buffer layers, which are invisible to synchrotron X-ray topography due to their poor crystal quality.

The strain between the InP ELO layers and the substrate was shown to be anisotropic due to the effect of the growth windows. The strain in the InP ELO layers was relaxed along the ELO stripes, but not in the direction perpendicular to the ELO stripes. This effect is probably not limited to the InP−InP−GaAs−Si material system, so similar anisotropy and small angle boundary structure may exist in various other ELO structures.

Acknowledgment. We thank Dr. Thomas Wroblewski for his assistance at HASYLAB beamline F1. This work was carried out with partial financial support from the Polish Committee for Scientific Research under Grant 3 T08A 021 26. Also, the support from SSF (Swedish Foundation for Strategic Research) is acknowledged.

References

(1) Zytkiewicz, Z. R. Laterally overgrown structures as substrates for lattice mismatched epitaxy. *Thin Solid Films* **2002**, *412*, 64−75.
(2) Sun, Y. T.; Baskar, K.; Lourdudoss, S. Thermal strain in indium phosphide on silicon obtained by epitaxial lateral overgrowth. *J. Appl. Phys. Commun.* **2003**, *94*, 2746−2748.
(3) Tuomi, T.; Naukkarinen, K.; Rabe, P. Use of synchrotron radiation in X-ray diffraction topography. *Phys. Status Solidi A* **1974**, *25*, 93−106.
(4) Sugo, M.; Yamaguchi, M. Buffer layer effects on residual stress in InP on Si substrates. *Appl. Phys. Lett.* **1989**, *54*, 1754−1756.
(5) Tuomi, T.; Synchrotron X-ray topography of electronic materials. *J. Synchrotron Radiat.* **2002**, *9*, 174−178.
(6) Sugo, M.; Uchida, N.; Yamamoto, A.; Nishioka, T.; Yamaguchi, M. Residual strains in heteroepitaxial III−V semiconductor films on Si-(100) substrates. *J. Appl. Phys.* **1989**, *65*, 591−595.
(7) Fang, S. F.; Adomi, K.; Iyer, S.; Morkoc, H.; Zabel, H. Gallium arsenide and other compound semiconductors on silicon. *J. Appl. Phys.* **1990**, *68*, 31−58.

CG0503301